

RESEARCH ARTICLE

Uncovering the mystery of Al(III) doping of ϵ -Fe₂O₃ in the ancient high-iron black-brown glaze

Ming Guan^{1,#} | Yu Guo^{2,#} | Baoqiang Kang¹ | Maolin Wang² | Gen Li¹ |
Yi Zheng³ | Yinzhong Ding¹ | Meng Wang² | Nigel Wood⁴ | Yong Lei¹  |
Xiangjun Wei³ | Ding Ma²

¹The Palace Museum, Beijing, P. R. China²Beijing National Laboratory for Molecular Sciences, College of Chemistry and Molecular Engineering, and BIC-ESAT, Peking University, Beijing, P. R. China³Shanghai Advanced Research Institute, Shanghai Synchrotron Radiation Facility, Chinese Academy of Sciences, Shanghai, P. R. China⁴School of Archaeology, University of Oxford, Oxford, UK

Correspondence

Yong Lei, The Palace Museum, Beijing,
100009, P. R. China.

Email: leiyong@dpm.org.cn

Xiangjun Wei, Shanghai Advanced
Research Institute, Shanghai Synchrotron
Radiation Facility, Chinese Academy of
Sciences, Shanghai, 201204, P. R. China.
Email: weixiangjun@sinap.ac.cn

Ding Ma, Beijing National Laboratory for
Molecular Sciences, College of Chemistry
and Molecular Engineering, and
BIC-ESAT, Peking University, Beijing,
100871, P. R. China.
Email: dma@pku.edu.cn

Funding information

National Natural Science Foundation of
China, Grant/Award Numbers: U1932203,
U1832164

Abstract

The world's first high-fired glazes were made in China, probably in the 16th century BCE, based largely on siliceous clay and calcareous wood ash. By the Song Dynasty (960–1279), this technology was at its zenith and included blackware glazes that exhibited reddish-brown single-phase, micron-scale ϵ -Fe₂O₃ films on their surfaces. However, it has been difficult to synthesize and replicate this effect on a larger scale and to a higher degree of purity through modern synthetic methods. To fully understand this effect, a strategy that combines nanomaterial science methods and theoretical calculation has been developed to study the hare's fur glazes of Song Dynasty (960–1279) Jian wares. Through our study of the original Song glazes, we show that a high-alumina clay was used in creating the glaze, which introduced Al into the ϵ -Fe₂O₃ lattices, playing a crucial role in metastable crystal stabilization. The explanation of both Al-doping from clay, combined with a new understanding of ancient but effective firing manipulation, may provide alternative approaches for materials synthesis.

KEYWORDS

Al(III) doping, clay, firing manipulation, hare's fur glaze, high-fired glaze, ϵ -Fe₂O₃

1 | INTRODUCTION

Clay, as the final product of the weathering of rocks, is mainly comprised of silica and alumina. When mixed with water, formed, dried, and then fired, the first synthetic material was created at least 20 000 years ago

in China.¹ Thereafter, when it was accidentally exposed to fly-ash (a flux) during wood firing, about 3500 years ago, a type of high-fired stoneware glaze was created. This glassy coat effectively improved the impermeable and waterproof properties of Chinese ceramics, as well as enhancing the material with both color and decoration.² This technology soon developed into the deliberate mixing of clays and wood ashes to make glazes

[#]Ming Guan and Yu Guo contributed equally to this work.

that could be applied directly to the raw wares before firing.

Differences in climatic and geological conditions between West and East Asia have resulted in separate developments in world ceramic history (Supporting Information Figure S1). The chemical differences between plants from hot arid or saline regions of the Near Eastern and temperate or subtropical regions of China, led to the creation of glazes based on high-soda ashes and high-calcia ashes, respectively. Such glazes have different maturing temperatures, and the high-temperature glazes characteristic of Chinese ceramics required firings of at least 1150°C, which is about 200°C higher than for Western glazes or glasses.³ Also, when producing glaze or glass, the western craftsmen preferred to use sands or crushed quartz pebbles rather than clay, as the materials' main siliceous component, which resulted in very low alumina levels in their compositions.⁴ These differences in both siliceous raw materials and glaze fluxes meant that Chinese high-alumina, high-calcia, and high-fired glazes presented a distinct and separate chemical reaction system, in which a series of specific reactions in silicate materials could be initiated. Thus, there are some unique types of glazes in China's high-fired glaze tradition, such as liquid in liquid separated glaze, sky-blue structurally colored glaze, and certain specific microcrystals such as ϵ -Fe₂O₃ created on high-iron black-brown glaze (iron oxide acting as the glaze colorant) through the firing process.⁵

1.1 | ϵ -Fe₂O₃, an advanced magnetoelectric material, on high-alumina, high-calcia, high-fired glaze

As one of the more representative crystallite-colored glazes, the ϵ -Fe₂O₃-colored black-brown glaze has attracted a high degree of academic attention. This is because ϵ -Fe₂O₃ is an advanced magnetoelectric material with an extremely large coercive field of 20 kOe at room temperature, significant ferromagnetic resonance, and coupled magnetoelectric features.^{6,7} However, existing synthetic approaches have held back a fuller exploration of ϵ -Fe₂O₃ as an advanced magnetoelectric material. So far, since 2010, when ϵ -Fe₂O₃ film was first prepared by modern chemistry, 100–200 nm-sized ϵ -Fe₂O₃ with low yield has been synthesized, although other iron oxide polymorph impurities were also present.^{7–9} Recently, by the introduction of rhodium doping into the ϵ -Fe₂O₃ lattice, an oriented ϵ -Fe₂O₃ film with a large coercive field of 45 kOe was prepared,¹⁰ which is the largest among magnetic ferrites to date, significantly enhancing the magnetic application of ϵ -Fe₂O₃. Even so, the convenient preparation of single-phase ϵ -Fe₂O₃ with high yield,

micron size, desired morphology, and stability, remains a considerable challenge for modern chemistry.

Interestingly, several new achievements in the study of ancient Chinese ceramics have confirmed that single-phase micron-scale ϵ -Fe₂O₃ films were achieved routinely in many high-fired Chinese porcelain glazes nationwide, over some 1000 years of production^{11–21} (Supporting Information Figure S2). Furthermore, the ϵ -Fe₂O₃ has only been identified in the period when high-alumina, high-calcia, and high-fired glazes, with high ratios of clay, were intentionally mixed with wood ash. Therefore, it seemed important to explore the mechanism of ϵ -Fe₂O₃ synthesis on clay-based high-fired glazes and to investigate the role of clay in ϵ -Fe₂O₃ crystallization and stabilization.

1.2 | ϵ -Fe₂O₃ performing gold or silver color on hare's fur glaze

Recent researches have reported that ϵ -Fe₂O₃ was the only chromogenic crystal form present on both gold and silver color strips or spots on a Song Dynasty hare's fur glaze,^{11,12} which belongs to the summit of high-iron black-brown glaze technology, but with the crystallites showing different sizes and shapes. This suggested that the craftsmen excelled at manipulating the physicochemical properties of their crystallites to create different colored glazes by virtue of ϵ -Fe₂O₃, particularly in the multicolored hare's fur glaze. However, the mechanism of how to control the details of firing (e.g., temperature, atmosphere, and holding time) to realize the crystal size, shape, or orientation of ϵ -Fe₂O₃ crystals, so that the glaze presented different optical performance, remained a great challenge.

In this work, a strategy was employed that combined material-science methods with theoretical calculation to investigate the role of clay-based high-fired systems in ϵ -Fe₂O₃ crystallization. The work also explored the role of firing manipulation in creating ϵ -Fe₂O₃ films on glazes with different optical performances. With the help of X-ray diffractometer (XRD) refinement and TEM-EDS, we found that Al(III) was doped in the ϵ -Fe₂O₃ lattice, leading to lattice compression, which was confirmed by Raman and extended X-ray absorption fine structures (EXAFS). Theoretical calculations were also performed to identify the influence of Al doping on the stability of the ϵ -Fe₂O₃ lattice. Meanwhile, using similar recipes and conditions, simulations were performed, and the outcomes were characterized. Based on the various strategies adopted, the results tested our hypotheses. It was found from this work that a uniform-sized, high-yielding, and oriented ϵ -Fe₂O₃ film was present on a silver hare's fur glaze. To understand this advanced firing technology, different manipulations for silver and gold-colored hare's fur glaze

were investigated and interpreted. In these cases, atmosphere, temperature, and synthetic rate all played vital roles, as evidenced by ionic Fe^{2+} dominating on the silver glaze surface rather than crystallographic $\varepsilon\text{-Fe}_2\text{O}_3$. This systematic and deep rediscovery of controllable synthesis of $\varepsilon\text{-Fe}_2\text{O}_3$ by using ceramic glazes has refreshed and enhanced our understanding of this clay-based high-fired ceramic system. The work showed that oriented $\varepsilon\text{-Fe}_2\text{O}_3$ synthesis was achieved with doping techniques more than 1000 years ago. This work may provide an innovative alternative approach for synthetic chemistry, as a gift from an ancient Chinese high-fired ceramic system.

2 | MATERIALS AND METHODS

A total of 23 hare's fur glazed sherds excavated from the Shuiji kiln in Fujian Province (Supporting Information Figure S3a) were grouped into silver and gold subtypes.²² With $\mu\text{-XRD}$, all samples were primarily analyzed, six of which were selected as representatives of silver (FJS-004 and FJS-006) and gold (FJS-005, FJS-007, FJS-008, and FJS-010) samples, respectively (Supporting Information Figure S3b-g). According to the kiln site survey, samples were believed to have been fired during the Southern Song Dynasty (12th–13th century). The glaze cross-sections were observed with a Leica DM4000 microscope.

Crystal identification was accomplished on the D8 Discover X-ray micro-diffractometer (Bruker) under $\text{Co K}\alpha$ ($\lambda = 1.79026 \text{ \AA}$) radiation with a 2D VANTEC-500 detector, operating at 40 kV, and tube current of 375 μA . A JEOL JEM-2100 TEM equipped with the LaB_6 gun was applied for TEM imaging, and selected area electron diffraction with operating voltage of 200 kV, and Oxford X-MAX energy dispersive X-ray spectrometer (EDS) for elemental analysis. Moreover, Raman spectra were obtained using the Invia 2000 laser confocal Raman spectrometer (Renishaw) with a 532 nm laser, an 1800 gr/mm dispersion grating, and a laser power of approximately 10 mW. Raman imaging was performed on a LabRAM HR Evolution Raman spectrometer (HORIBA) with a 532 nm laser, laser power of 1 mW, a 600 gr/mm dispersion grating, and a step size of $0.4 \times 0.4 \mu\text{m}^2$.

X-ray absorption spectroscopy (XAS) of Fe K edge (7112 eV) were obtained at the BL14W1 beamline of the Shanghai Synchrotron Radiation Facility at 3.5 GeV with a maximum current of 300 mA with a Si (111) double-crystal monochromator. X-ray photoelectron spectroscopy (XPS) was performed on an Axis Supra imaging photoelectron spectrometer (Kratos) with Al $\text{K}\alpha$ quartz monochromator source operating at 150 W. An MR-351 constant-acceleration Mössbauer spectrometer (FAST) driven with a triangular reference signal was utilized at 10 K, with a ^{57}Co

radioactive source in the Rh matrix. The values of isomer shifts were relative to the ones of $\alpha\text{-Fe}$ foil at 10 K.

SEM analysis was performed on MIRA 3-FE-SEM (TESCAN). The BSE images were obtained at 20 kV and a beam intensity of 18.0, with a spot size of approximately 8 nm. Microphotographs were captured six times and 300 particles were selected for size distribution analysis. For SEM-EBSD, binning was set as 4×4 under the enhanced mode.

Spin-polarized density functional theory (DFT) calculations were carried out using the Vienna Ab initio Simulation Package.²³ The generalized gradient approximation method and the exchange-correlation functional developed by Perdew, Burke, and Ernzerhof²⁴ were used with projected augmented wave potentials²⁵ for electron-ion interactions. The DFT + U method was applied in this work. Detailed information is available in Supporting Information.

3 | RESULTS AND DISCUSSION

3.1 | Al doping was discovered in $\varepsilon\text{-Fe}_2\text{O}_3$ lattices on hare's fur glaze

$\mu\text{-XRD}$ characterization identified streak compositions and indicated that doped $\varepsilon\text{-Fe}_2\text{O}_3$ was on the streaks of silver and gold hare's fur glazes (Figure 1A and Supporting Information Figure S4), in which FJS-004 for silver glaze and FJS-007 for gold glaze were typical. There were peaks of 32.55° (022), 35.40° (013), 38.65° (122), 41.25° (200), and 42.85° (131) for FJS-004 and those of 32.50° (022), 35.45° (013), 38.65° (122), 41.20° (200), 43.10° (131), 48.90° (212), and 62.95° (051) for FJS-007, which were approximately in accord with the reference pattern of $\varepsilon\text{-Fe}_2\text{O}_3$, but entirely shifted to higher angles, as revealed by the right panel in Figure 1A. It can be observed that the (122) peak of $\varepsilon\text{-Fe}_2\text{O}_3$ reference (specimen from Pleistocene basaltic scoria) was located at 38.4° , while that for FJS-004 and FJS-007 had shifts of 0.2° and 0.4° , respectively. More interestingly, these shifts were enlarged in higher 2θ degrees, for example, the (132) peak had shifts of 0.3° and 0.7° compared to the reference. Instead, the (122) peak of $\text{Al}_{0.31}\text{Fe}_{2.35}\text{O}_4$ reference was 38.7° , lying closer to that of FJS-004 and FJS-007. Obviously, the $\varepsilon\text{-Fe}_2\text{O}_3$ on both hare's fur glazes were closer in their nature to natural Al-doping luogufengite than to that seen in synthetic materials.

Moreover, $\text{Al}_{0.31}\text{Fe}_{2.35}\text{O}_4$, Al(III) doped into $\varepsilon\text{-Fe}_2\text{O}_3$ lattices had a smaller ion radius than Fe(III), giving rise to the shrinkage of $\varepsilon\text{-Fe}_2\text{O}_3$ lattices and a diffraction peak shift towards higher angles. For FJS-004 and FJS-007, the shifts would also result from certain dopants with a smaller ionic radius, largely due to the reaction of Fe precursors

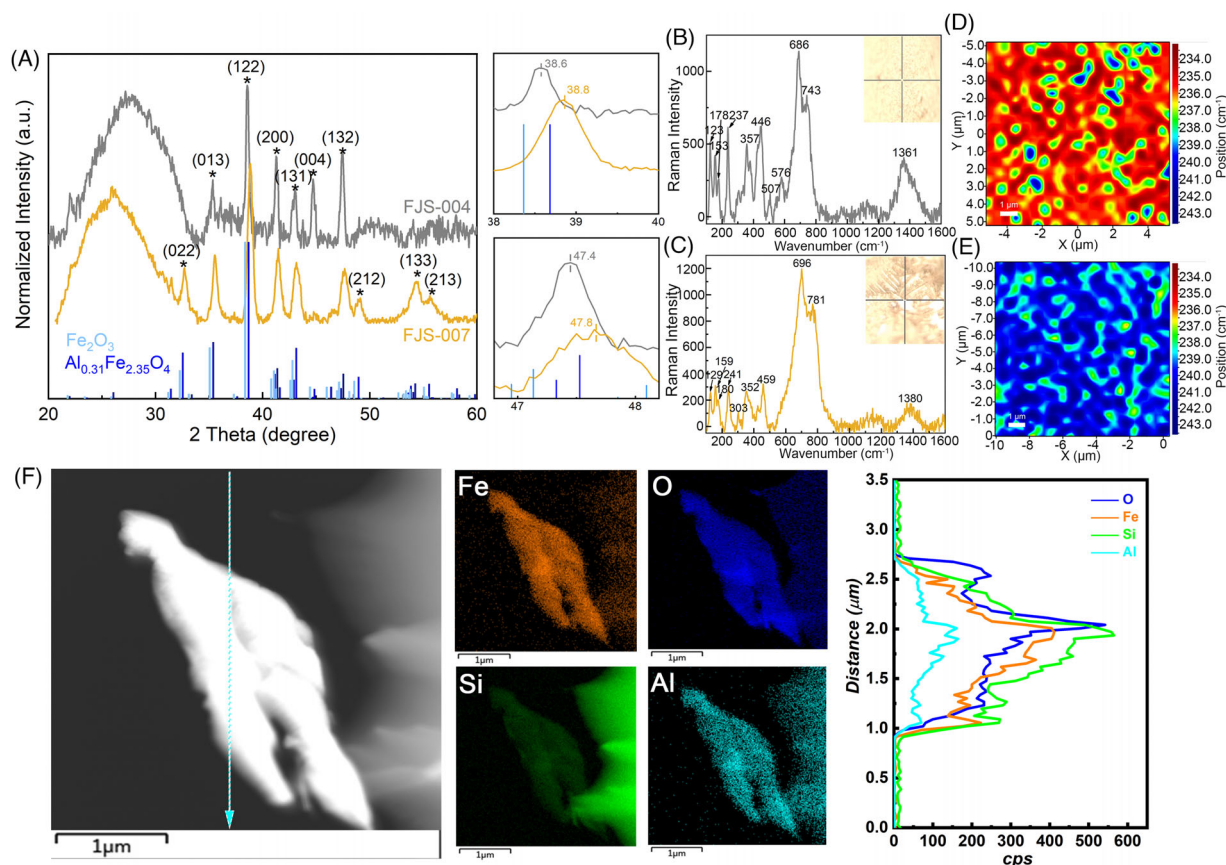


FIGURE 1 The evidence for the introduction of Al-doping in ϵ -Fe₂O₃ lattices on hare's fur glazes. (A) The XRD spectra of FJS-004 and 007 compared with ϵ -Fe₂O₃ standards. (B,C) The Raman spectra of FJS-004 and FJS-007. (D,E) The two-dimensional Raman images of FJS-004 and FJS-007. (F) The elemental distribution and line scan of ϵ -Fe₂O₃ crystals based on TEM-EDS mapping at nanometric scales.

and other ingredients during high-temperature firing processes. The XRD patterns were further fitted by Rietveld refinement to give the lattice parameters of ϵ -Fe₂O₃ crystals (Supporting Information Figure S5 and Table S1). It is known that ϵ -Fe₂O₃ is orthorhombic with the space group of Pna21. The obtained lattice parameters of *a*, *b*, and *c* are listed in Supporting Information Table S1, in which FJS-004 and FJS-007 had increasingly evident lattice compression, showing that ϵ -Fe₂O₃ lattices in silver and gold glazes were increasingly compressed, possibly owing to doping with a smaller radius than Fe(III).

In practice, it seems reasonable to assume that Al(III) doping could be introduced into ϵ -Fe₂O₃ lattices by the following clues. On one hand, the hare's fur glaze belongs to the Chinese high-fired ash glaze (CaO(MgO)-K₂O(Na₂O)-Al₂O₃-SiO₂ system), exhibiting high alumina levels (about 16 wt%Al₂O₃ in the glaze composition), achieved through the use in the glaze of a high-alumina clay.³ This was substantially more Al₂O₃ than in Middle Eastern Islamic low-fired alkaline glazes or in western glass. However, it was worth noting that ϵ -Fe₂O₃ was also found in archaeological baked clay materials in Europe, but with α -Fe₂O₃ impurities and a low yield,²⁶ which again demonstrated

the crucial role of the Chinese clay-based system with its more specific chemical composition. On the other hand, at the atomic scale, the ionic radius of Al³⁺ (53.5 pm) was close to that of Fe³⁺ (64.5 pm), which provided the capability for Al(III) substitution of Fe(III) in ϵ -Fe₂O₃. Further, Al substitution has also been applied as a strategy for ϵ -Fe₂O₃ preparation in synthetic chemistry.²⁷ Therefore, it was well-founded to hypothesize that Al(III) may be doped in ϵ -Fe₂O₃ lattices where it performed the role of a stabilizer to create single-phase, high-yield, micron-scale ϵ -Fe₂O₃ on the glaze surface. Of course, the effect may not have been intentionally designed, but was recognized and repeated, resulting in amazing outcomes within the Chinese high-fired system.

To probe into the ϵ -Fe₂O₃ lattices on hare's fur glazes, Raman spectra were collected over different samples (Figure 1B-e), with the peaks of 123, 153, 178, 237, 357, 446, 507, 576, 686, 743, and 1361 cm⁻¹ for ϵ -Fe₂O₃ on FJS-004 and 129, 159, 180, 241, 303, 352, 459, 696, 781 and 1380 cm⁻¹ for those on FJS-007. The peaks were generally in accord with the published ϵ -Fe₂O₃ Raman spectra.¹¹ It has been well established that the Raman peaks at 123, 685, and 730 cm⁻¹ correspond to first-order phonon modes, and variations of

their band positions and widths would indicate changes in lattice stress. Therefore, the Raman spectra were fitted to give the full width at half maximum (FWHM) and the wavenumber at presumably 123, 685, and 730 cm^{-1} (Supporting Information Figure S6 and Table S2). It can be seen that FJS-004 peaked at 125, 690, and 754 cm^{-1} , while FJS-007 at 129, 699, and 786 cm^{-1} , showed notable shift toward higher wavenumbers than the former. The two-dimensional Raman images confirmed the blue shift of Raman bands for FJS-007 at microscale. Given that there were no new peaks sorted for FJS-007, compared to FJS-004, the blue-shifted peaks suggested the more compressed $\epsilon\text{-Fe}_2\text{O}_3$ lattice for FJS-007,²⁸ which was consistent with the $\mu\text{-XRD}$ results. In addition, FJS-007 had larger FWHM values than FJS-004 for the three fitted peaks, possibly due to the higher content of Al in the $\epsilon\text{-Fe}_2\text{O}_3$ lattice in FJS-007, as indicated by the elemental composition in Supporting Information Table S3.

Furthermore, the introduction of Al doping in $\epsilon\text{-Fe}_2\text{O}_3$ lattices was confirmed via TEM observations. Samples were primarily prepared by FIB (Supporting Information Figure S7). The elemental compositions of dendritic crystals were analyzed based on TEM-EDS (Supporting Information Table S3), indicating that the crystals on the silvery and gold streaks were comparatively enriched with the Fe relative amount of 36–57 wt%, which were presumed to be iron oxides. It should be noted that there were also considerable amounts of Si, Al, and Ca elements, which may stem from the substrate or doping element of the lime glaze. The elemental distribution was detected by TEM-EDS mapping at nanometric scales (Figure 1F). It can be seen from this that the Fe element was predominantly distributed within dendritic crystals, and Al coexisted within these crystals, as clearly demonstrated in the line scan results. Therefore, the Al element appeared to be doped into $\epsilon\text{-Fe}_2\text{O}_3$ crystals, which derived from the ancient Chinese method of using Al-rich clay in the glaze, while Si may derive from the clay.

Simulations preparation of $\epsilon\text{-Fe}_2\text{O}_3$ with the hare's fur glaze recipe (Supporting Information Table S4) and conditions were also performed. This confirmed our opinion that lattice compression existed in high-fired $\epsilon\text{-Fe}_2\text{O}_3$ on the glaze, possibly due to Al doping (Supporting Information Figure S8). As can be seen, $\mu\text{-XRD}$ results of $\epsilon\text{-Fe}_2\text{O}_3$ crystals on simulated silvery-black and gold glazes also shifted to higher angles, for instance, the peak (122) were 0.2–0.4° higher than $\epsilon\text{-Fe}_2\text{O}_3$ reference, but more like $\text{Al}_{0.31}\text{Fe}_{2.35}\text{O}_4$ reference, which was in accord with the results of archaeological samples. Moreover, according to the latest study, Al-substituted $\epsilon\text{-Fe}_2\text{O}_3$ was also found on a Japanese Bizen stoneware replica, which is widely believed to be profoundly influenced by Chinese high-fired black-glazed tea cups.²⁹

3.2 | $\epsilon\text{-Fe}_2\text{O}_3$ lattices were stabilized by the introduction of Al doping

To simulate the effect of Al doping on $\epsilon\text{-Fe}_2\text{O}_3$ crystals, a theoretical calculation was performed on $\epsilon\text{-Fe}_2\text{O}_3$ lattices. According to lattice parameters from XRD refinement, the compressed a, b, and c values for orthorhombic $\epsilon\text{-Fe}_2\text{O}_3$ in FJS-004 were 99.2, 97.2, and 98.1% of those in relaxed $\epsilon\text{-Fe}_2\text{O}_3$ structure, and the ones in FJS-007 were 98.7, 96.9, and 97.3% of those in relaxed structure, respectively. It was supposed that Al doping would cause such compression, thus, models with different ratios of Al dopants were built based on the optimized $\epsilon\text{-Fe}_2\text{O}_3$ structure with no lattice strain. The elemental composition of the primitive $\epsilon\text{-Fe}_2\text{O}_3$ cell was $\text{Fe}_{16}\text{O}_{24}$. A total of one to four Al atoms were doped into the lattice, corresponding to a doping ratio from 6.25 to 25% (Figure 2A). It should be noted that the doping ratio of the XRD reference of $\text{Al}_{0.31}\text{Fe}_{2.35}\text{O}_4$ was 12%, which was within the calculated doping ranges.

The most stable structures of Al-doped $\epsilon\text{-Fe}_2\text{O}_3$ lattices are represented in Figure 2B. With one to four Al atoms replacing Fe atoms, different doped structures were built and computed to select the most stable, with the least formation energy (Supporting Information Figure S9). The lattice parameters of the Al-doped structures are displayed in Supporting Information Table S5, from which a, b, and c values decreased with the increase of Al doping ratios (Figure 2A), validating the conclusion from experimental results that Al doping would induce lattice compression. However, the ratios of lattice parameters for $\text{Al}_4\text{Fe}_{12}\text{O}_{24}$ in the b and c direction to those of undoped Fe_2O_3 structures were still larger than the actual ratios for FJS-007, indicating that subtle differences existed between computational and experimental results.

Crystal orbital Hamilton population (COHP) has been an effective descriptor for bonding and antibonding interactions within solid materials. By integrating the COHP of an Fe-O bond up to the Fermi level, the contribution of the Fe-O bond to the band-structure energy can be obtained, from which the bond strength can be indicated. Therefore, the integrated COHP values were calculated for models with different Al doping ratios (Figure 2B). The values grew more negative with the increase of Al doping ratio up to 18.75%, demonstrating the enhanced bond strength for the Fe-O linkage in increasingly compressed Fe_2O_3 lattices. However, when further lifting the doping ratio to 20%, the integrated COHP value became less negative, indicating the disadvantageous influence of excess Al ions on the Fe-O bonding strength in Fe_2O_3 lattices. Therefore, a suitable doping ratio of Al ions would strengthen the Fe-O bonds and possibly contribute to the stabilized $\epsilon\text{-Fe}_2\text{O}_3$ crystals on glaze.

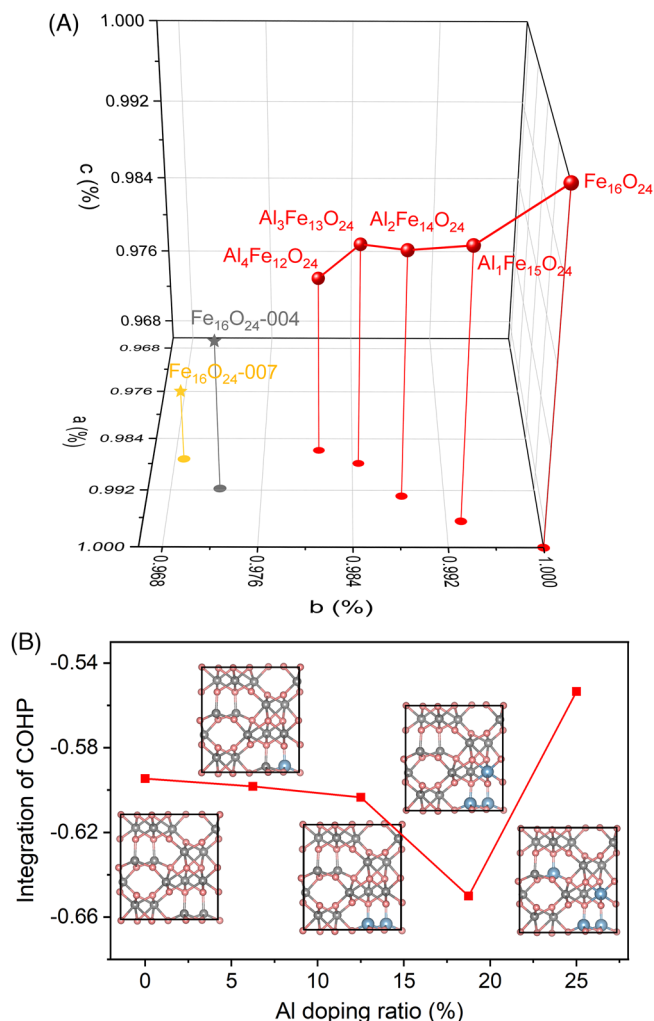


FIGURE 2 Theoretical calculations of Al-doped ϵ -Fe₂O₃ lattices. (A) The compressed lattice parameters for Al-doped ϵ -Fe₂O₃ models with different Al doping ratios, in which the compressed ratios for FJS-004 and FJS-007 from refined lattice parameters were also indicated. (B) The variation of integrated COHP with different Al doping ratios, in which the most stable structures of the corresponding Al-doped ϵ -Fe₂O₃ lattices were displayed. The Fe, O, and Al atoms were represented with grey, pink and blue spheres.

3.3 | The advanced manipulation succeeded in preparing a uniform-sized, high-yield, oriented ϵ -Fe₂O₃ film on silver hare's fur glaze

The other important task of this work was to assess how the ancient but advanced firing manipulation succeeded in preparing ϵ -Fe₂O₃ film with different optical performances on the glazes. This was elucidated by comparative research on silver and gold hare's fur glazes. It should be noted that, in the archaeological samples studied, we also found a number of hare's fur sherds with yellowish-brown dull-surfaced streaks (FJS-008 and FJS-010), which were classified as gold glaze because of their similar appearance

and general classification by archeologists, although their reflectance spectra and color parameters (especially for the *L* value) differed considerably (Supporting Information Figure S10 and Table S6).

First and foremost, the surface morphology of ϵ -Fe₂O₃ crystals was compared with silver and gold hare's fur glazes, indicating that a thin layer of ϵ -Fe₂O₃ with uniform size distribution and high yield was stabilized on the silver glaze, which matched the special metallic reflective effect. To gain insights into the ϵ -Fe₂O₃ crystals on the glaze, the glaze cross-section was observed (Figure 3A–C), indicating that ϵ -Fe₂O₃ was located on the topmost layer of the glaze, with thicknesses of about 10, 15–60, and 20–50 μ m for FJS-004, FJS-007, and FJS-010, respectively. The morphology, size distribution, and coverage of crystals can be observed by SEM (Figure 3D–F and Supporting Information Figure S11). For FJS-004 and FJS-006 as the representatives of silver hare's fur glaze, crystals shaped as a dendrite with four to six branches, and the sizes were $1.72 \pm 1.14 \mu$ m and $1.44 \pm 0.44 \mu$ m, with the coverage of 72.43 and 67.11%, respectively. In contrast, FJS-007 and FJS-005, as the representatives of gold glaze, were also covered by dendritic crystals, with the size of 2.98 ± 1.72 and $14.45 \pm 7.55 \mu$ m and crystal coverage of 62.24 and 65.33%, respectively. Strikingly, large dendritic crystal clusters were randomly distributed on FJS-008 and FJS-010 with the size of 20.71 ± 7.04 and $20.18 \pm 7.52 \mu$ m. It can be seen that the size of ϵ -Fe₂O₃ crystals on the glaze was increased from the silver to the gold glaze, with successively decreased crystal coverage.

Moreover, SEM–EBSD was applied to mapping ϵ -Fe₂O₃ orientation distribution on FJS-004 and FJS-007 (Figure 3 G,H), which was considered to be related to the intensity of the metallic reflection. For FJS-004, three different places were randomly selected to investigate ϵ -Fe₂O₃ orientations on glaze surface (Figure 3G and Supporting Information Figure S12a–c). Inverse Pole Figure (IPF) maps suggested that the larger-grained ϵ -Fe₂O₃ on FJS-004 displayed as purple or red had unique orientations, which was also proved by the distribution of crystal planes along with [001] crystal direction in the inset graph. In comparison, ϵ -Fe₂O₃ orientations on FJS-007 were randomized and crystal planes were also randomly distributed (Figure 3H and Supporting Information Figure S12d). Summarily, the SEM–EBSD results indicated that ϵ -Fe₂O₃ on the silver glaze was uniquely oriented, while that on the gold glaze was randomly precipitated. Oriented growth of crystals on glaze has been proved to play an important role in presenting the metallic and luster effect of glaze, which has been reported not only in CeO₂-opacified glisten glaze of modern ceramics³⁰ but also in α -Fe₂O₃-based roofing tile glaze.³¹ In our case, assuming that ϵ -Fe₂O₃ crystals were distributed with specific orientations on the silver

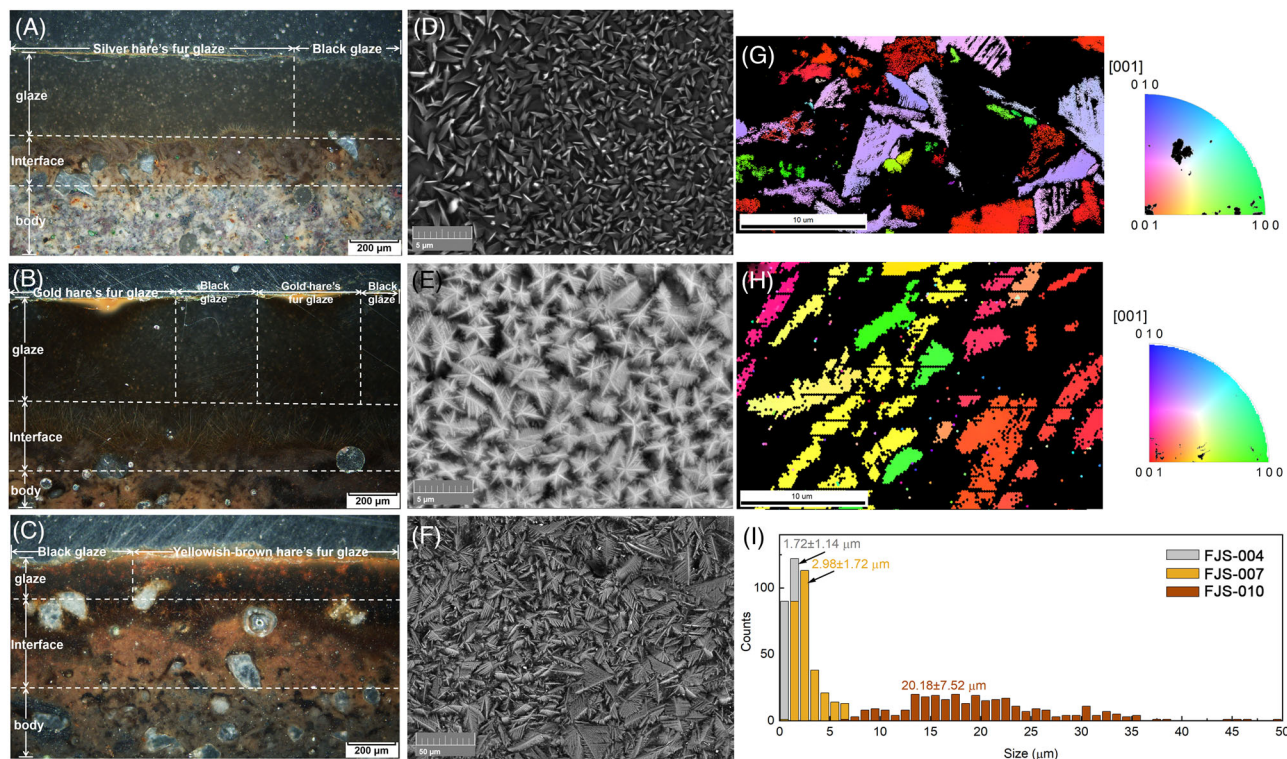


FIGURE 3 The uniform-sized, high-yield, oriented ϵ -Fe₂O₃ film was stabilized on silver hare's fur glaze. (A–C) The cross-sections of FJS-004, 007, and 010. (D–F) The BSE images of FJS-004, 007 and 010. (G,H) The inverse pole figure (IPF) graph showing orientation distribution of ϵ -Fe₂O₃ on the surface of FJS-004 and FJS-007, with the distribution of crystal planes along with the [001] crystal direction in the right panels. (I) The size distribution of ϵ -Fe₂O₃ on three glazes.

glaze, when the incident light is illustrated on the glaze, the reflected light may reflect within certain directions, representing as the metallic effect.

Combined with BSE images and electron backscattered diffraction (EBSD) results, it was demonstrated that a uniform-sized, high-yield, oriented ϵ -Fe₂O₃ thin film was synthesized on the silver surface of hare's fur glaze. This caused a metallic reflective effect on the glaze based on the subtle firing manipulation, which was more convenient and efficient than the modern synthetic method. The ϵ -Fe₂O₃ on the silver streaks was formed as dendritic crystals, similar to those on the gold streaks, but with specific orientation, a small size and high crystal coverage (Figure 3D–I); while for the ϵ -Fe₂O₃ on the gold glaze, the size was larger and the crystal coverage lower than that on the silver one, with the metallic effect weakened.

3.4 | The clues of advanced firing manipulation were uncovered on hare's fur glaze with multiple optical performance

To reveal the subtlety of this ancient technology, a series of material-science investigations were employed. First and foremost, the coordination and valence of Fe centers in ϵ -

Fe₂O₃ on silver and gold hare's fur glazes were compared, and their roles in coloration were elaborated. The Fe K-edge XAS experiments were conducted to determine the valences and coordination of Fe centers in the bulk phase. The near-edge structures are displayed in Figure 4A. The FJS-004, FJS-007, and FJS-010 all had higher energies of the absorption edges than the Fe₂O₃ standard, but lower than the FeO standard, indicating the three samples all had Fe²⁺ ions in their ϵ -Fe₂O₃ lattices. Besides, the pre-edge peak at 7113 eV was ascribed to 1s→3d transition,³² which was electric dipole forbidden, but would be possible due to the allowed electric quadrupole transition. The increased intensity of pre-edge peak for the three samples studied, compared with the Fe₂O₃ standard, suggested the decreased coordination number (CN) of Fe center atoms was most likely due to the presence of tetrahedral coordinated Fe sites. It has to be mentioned that ϵ -Fe₂O₃ had four types of Fe sites and six types of O sites.³³ Fe_AO₆ and Fe_BO₆ are largely distorted octahedral; Fe_CO₆ is regular octahedral and Fe_DO₄ is tetrahedral. The intrinsic tetrahedral coordinated Fe sites in ϵ -Fe₂O₃ lattices would also give rise to the predominant pre-edge peaks.

The Fourier transform of EXAFS gave more coordinated information of Fe center atoms. From Figure 4B, Supporting Information Figure S13, Table S1, and Table

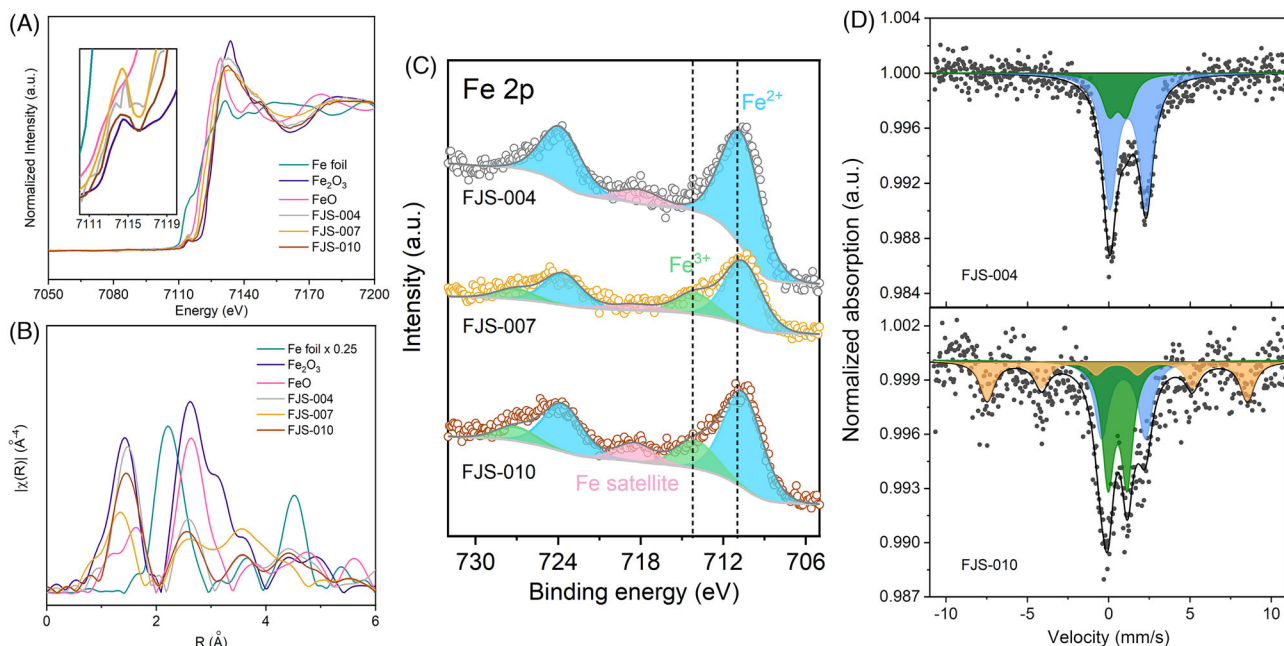


FIGURE 4 The clues of firing conditions revealed from the valence and coordination of Fe centers in the ϵ - Fe_2O_3 of glazes. (A) The Fe K-edge XANES spectra of glazes. (B) The Fourier transform of EXAFS signals. (C) The Fe 2p XPS spectra and deconvoluted peaks of Fe^{2+} (blue), Fe^{3+} (green), and Fe satellite (pink). (D) Mössbauer spectroscopy of FJS-004 and FJS-010, in which blue doublet indicated paramagnetic Fe^{2+} state, green doublet represented paramagnetic Fe^{3+} state, and orange sextet signified Fe octahedral sites in ϵ - Fe_2O_3 lattices.

S7, FJS-007 had a CN of 6.4 ± 1.8 for the Fe-O shell and 4.5 ± 3.4 for the Fe-Fe shell, which were quite close to the CNs of 6.0 and 4.0 for the Fe-O and Fe-Fe shells of Fe_2O_3 standard, respectively. However, the Fe-O bond length (R) for FJS-007 was 1.93 ± 0.03 Å, shorter than that of Fe_2O_3 standard sample of 1.99 ± 0.09 Å. The similar CNs but shorter bond lengths indicated a compressed ϵ - Fe_2O_3 lattice for FJS-007, in accordance with the results of μ -XRD and Raman characterizations. By contrast, FJS-004 and FJS-010 had much smaller CNs for the Fe-O shell, which are 4.5 ± 0.6 and 4.7 ± 0.6 , respectively, but similar Fe-O bond lengths with Fe_2O_3 standard. The sizes of ϵ - Fe_2O_3 in FJS-004 and FJS-010 were both large enough to exclude the effect of crystal size on Fe-O coordination. Therefore, the much-decreased Fe-O CNs revealed that there were some intrinsic differences between different ϵ - Fe_2O_3 lattices.

Having recognized that the three samples had Fe^{2+} in ϵ - Fe_2O_3 lattices, Fe 2p XPS signals were detected over FJS-004, 007, and 010, the results of which were also consistent with the above. As shown in Figure 4C, the Fe 2p 3/2 peak for FJS-004 had a binding energy of 710.66 eV, which was deconvoluted to show only Fe^{2+} signal. To confirm the sole presence of Fe^{2+} in silver glaze, the XPS spectra of FJS-006 were also recorded on the silver streaks (Supporting Information Figure S14). It turned out that the surface was all existed as Fe^{2+} with no Fe^{3+} . For FJS-007 and FJS-010, there appeared shoulder peaks at higher binding

energies, and peaks were deconvoluted to be a combination of both Fe^{2+} and Fe^{3+} signals, which centered at 710.55 and 714.03 eV for FJS-007 and 710.56 and 713.98 eV for FJS-010, respectively. The contents of Fe^{2+} on the surfaces were calculated based on the integrated areas of the Fe 2p signals, which turned out to be 100, 75, and 77% for FJS-004, FJS-007, and FJS-010 samples, respectively, indicating the reduced Fe^{2+} contents from FJS-004 to FJS-010 and FJS-007, and the gradual appearance of Fe^{3+} on the surface.

Complementary to the surface information from XPS, the ratios of different Fe states in the bulk of ϵ - Fe_2O_3 can be shown through Mössbauer spectroscopy. It has been verified that four types of crystallographic Fe sites in ϵ - Fe_2O_3 should show sextet signals with different intensities of hyperfine field.³⁴ In this work, four sextets were indistinguishable, and only one sextet was fitted (Figure 4D). It turned out that only two sets of doublets could be observed for FJS-004, with no sextet signals. The doublet³⁵ with IS and quadrupole splitting of 1.17 and 2.24 mm/s was ascribed to paramagnetic Fe^{2+} , accounting for 76.7% of the total Fe sites, while the one with values of 0.55 and 1.05 mm/s was due to paramagnetic Fe^{3+} with a proportion of 23.3% (Supporting Information Table S8). By contrast, FJS-010 (or FJS-007) had 29.7% (or 25.3%) of Fe^{2+} and 38.9% (or 48.6%) of Fe^{3+} , in addition to 31.4% (or 26.1%) of crystallographic Fe sites. The sextet of Fe sites in ϵ - Fe_2O_3 lattices had an increasing hyperfine field from 49.7 to 50.8 T as

varied from FJS-010 to FJS-007, indicating the increased lattice distortion. Thus, the bulk of the silver hare's fur glaze was again proved to have more Fe^{2+} than the gold one. The ionic Fe^{2+} would dominate in the Fe sites in the silver glaze rather than the crystallographic $\epsilon\text{-Fe}_2\text{O}_3$, while the latter would also take up a large proportion for the gold glaze.

From the above observations, the variation of light absorption for different glazes would be a consequence of the change in $\epsilon\text{-Fe}_2\text{O}_3$ band gap, or the ligand field splitting of Fe center atoms.^{36,37} Significantly, both the introduction of Fe^{2+} and lattice compression of $\epsilon\text{-Fe}_2\text{O}_3$ would affect band structures and induce a change of absorption or reflection wavelength. The $\epsilon\text{-Fe}_2\text{O}_3$ lattice was compressed for both silver and gold glazes, with more evident compression for the latter (Figure 1), resulting in gradually decreased Fe-O bond lengths and the strengthened Fe-O interaction from the silver to the gold glaze, as verified by theoretical simulation (Figure 2B). Additionally, XPS signals strikingly indicated that only Fe^{2+} existed on the silver glaze, and Fe^{3+} appears in the gold glazes (Figure 4C), which was also confirmed by Mössbauer spectroscopy (Figure 4D). The predominance of Fe^{2+} in the silver glaze may be due to the diluted CO atmosphere produced by incomplete wood burning during the firing process. As simply judged from the ligand field splitting, the splitting energy would be enlarged due to the high-valence state of the Fe center atoms and strengthened Fe-O interaction. Thus, the predominance of Fe^{2+} on the surface and the longer Fe-O bond length in $\epsilon\text{-Fe}_2\text{O}_3$ lattices both contributed to a smaller splitting energy for the silver glaze,^{36–39} resulting in the light absorption of longer wavelengths and the reflection of shorter wavelengths, which corresponded to the reflectance spectra. According to the theory of ligand field splitting, the interaction between 3d orbitals of center Fe ions and 2p orbitals of surrounding O ions would cause the splitting of the energy levels for Fe,³⁶ and the splitting energy would be reciprocally proportional to the 5th power of bond length r ($\sim 1/r^5$).^{37–39} Hence, a longer Fe-O bond length contributes to smaller splitting energy. However, we verify in our work that $\epsilon\text{-Fe}_2\text{O}_3$ can be doped with Fe^{2+} and Al^{3+} . In addition to Fe-O bond length, the content of Fe^{2+} and Al^{3+} can both contribute to the change of Fe's local environment, and also the absorption and reflection wavelength differences for different samples. There would be no direct correlation between the Fe-O bond length and the adsorbed or reflected wavelengths.

From the above studies, ionic Fe^{2+} on the glaze and its ratio to crystallographic $\epsilon\text{-Fe}_2\text{O}_3$ illustrate the unique firing manipulation achieved for different hare's fur glazes, especially regarding kiln atmosphere control. From the aspect of firing processes, it was reported that the sil-

ver glaze was fired under a reductive atmosphere, while the gold ones were fired under an oxidative atmosphere,⁵ which was consistent with the XPS and Mössbauer spectra, where Fe^{2+} dominated on the Fe sites in the silver glaze. Moreover, the temperatures used to sinter the ceramic bodies were measured to be 1262 and 1244°C for FJS-004 and FJS-006, 1321°C for FJS-007, respectively (Supporting Information Figure S15), which again suggested that a reductive atmosphere was applied in the silver glaze firing process since sintering temperature in reductive atmosphere was 55–80°C lower than that in an oxidative one. Therefore, silver streaks can be only produced under CO-rich reductive atmosphere and at an appropriate temperature. The Fe_2O_3 ingredients for silver glaze were supposed to undergo pyrolysis above 1240–1260°C, from which oxygen would be released as bubbles. The oxygen bubbles grew and rose to the glaze surface, carrying the remaining iron atoms from the Fe_2O_3 ingredients.⁴⁰ Once reacted with the reductive atmosphere on the surface, the iron would retain as Fe^{2+} , and precipitate together with Fe_2O_3 during the cooling process (Figure 5). By contrast, the oxidative atmosphere for gold glaze would induce Fe^{3+} on the surface. Moreover, with the higher kiln temperature in the O_2 -rich oxidative atmosphere, the pyrolysis reaction would be more violent, leading to more iron atoms rising up with the bubbles and later precipitating as $\epsilon\text{-Fe}_2\text{O}_3$, not only on the surface but also inside the glaze, as shown in TEM images (Supporting Information Figure S16).

On the other hand, the distinct size distribution, orientation, and unique crystallization of $\epsilon\text{-Fe}_2\text{O}_3$ contributed to the metallic-like reflective effect on the glaze, dependent on the overall influence of the kiln atmosphere, firing temperature, oxygen pressure, as well as holding and cooling times. The above conditions were all manipulated within one firing but succeeded in producing hare's fur glazes with different colors.

Summarily, our study also elaborated the coloration in hare's fur glazes, which was determined by both the diffuse reflection effect via Fe ligand field splitting and also by the metallic-like reflection effects from distinct size-distributed and oriented $\epsilon\text{-Fe}_2\text{O}_3$, achieved through unique manipulation of the firing process.^{41,42}

4 | CONCLUSIONS

In summary, the present study uncovered the role that high-alumina clay played in the single-phase micron-scale $\epsilon\text{-Fe}_2\text{O}_3$ synthesis on hare's fur glaze surface and how to realize multiple optical performance through this ancient but advanced high-temperature manipulation technology. On the one hand, the introduction of Al doping

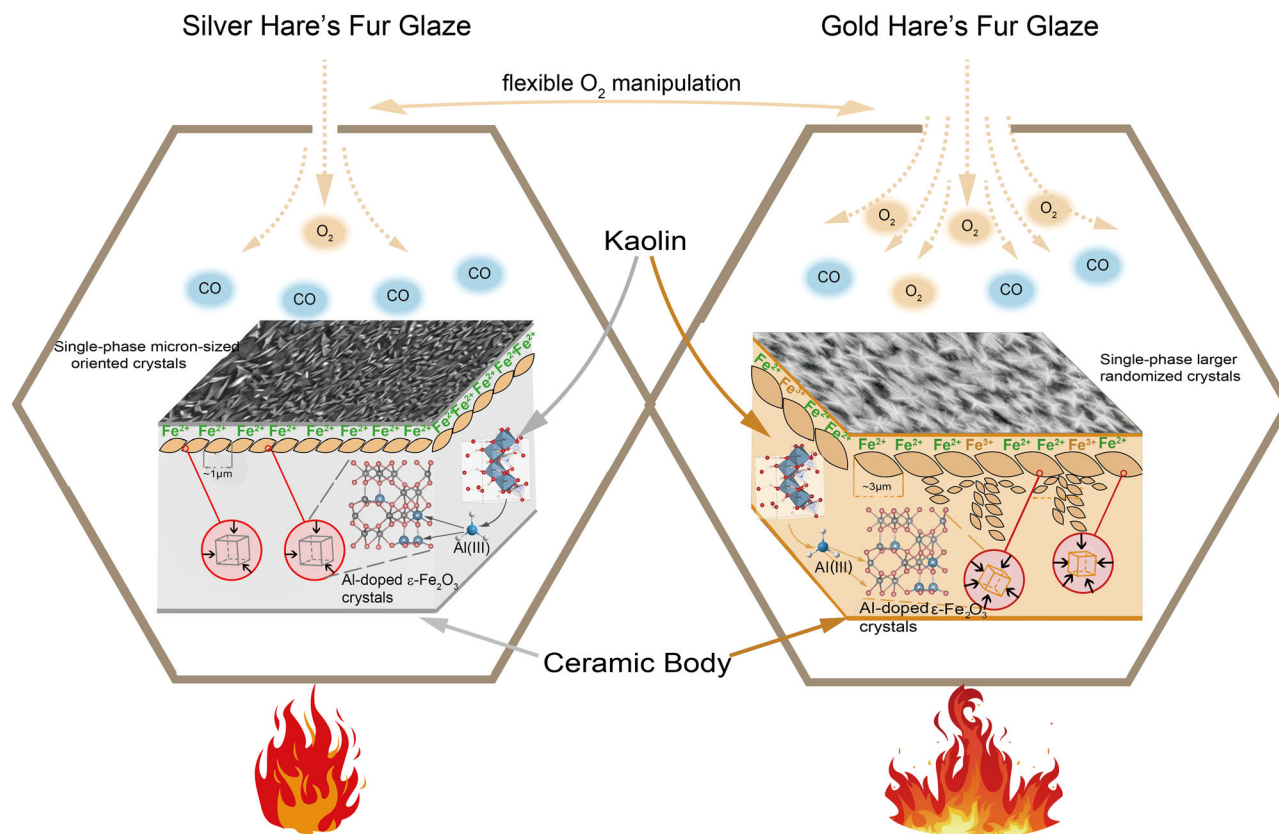


FIGURE 5 The manipulation of firing process of silver and gold hare's fur glazes. Uniform-sized, high-yield and oriented ϵ - Fe_2O_3 film was created on silver hare's fur glaze, while larger-sized randomized ϵ - Fe_2O_3 film on gold glaze, by the subtle but different control of atmosphere and firing environment.

was discovered to play a vital role in stabilizing ϵ - Fe_2O_3 lattices, which benefited from the use of high-alumina clay in the lime glaze of the Chinese high-fired ceramic system. On the other hand, an important discovery is that Chinese ancient craftsmen were skilled at kiln atmosphere control and the appropriate firing temperature to produce a uniform-sized, high-yield, oriented ϵ - Fe_2O_3 film on the silver hare's fur glaze.

In addition, a novel strategy combining various methods based on XRD refinement for lattice structure, XPS and Mössbauer spectroscopy for valence identification, and theoretical calculation has been applied for the first time in a deep investigation of doped crystals on Chinese high-fired glazes, which should broaden the methodology for ancient ceramics study. Additionally, the rediscovery of controllable synthesized ϵ - Fe_2O_3 , based on an ancient Chinese high-fired ceramic system, may provide an innovative paradigm in modern chemical synthetic methods, which should also bridge the two methodologies.

ACKNOWLEDGEMENTS

The authors wish to thank Guanqun Luo from the Jianyang City Museum for providing the samples, Dr. Xingwu Liu from Synfuels China for the measurement

of Mössbauer spectroscopy, Pinger Song from University of Science and Technology Beijing for the characterization of stimulated samples, Peiquan Duan, Cui Jia, Yuan Li, and He Li from the Palace Museum for taking part in data analysis and providing imitated samples, Xinyi Wang from the Palace Museum for the design and improvement of figures, and HORIBA Co. (China) and EDAX Co. (China) for the assistance in Raman mapping and EBSD analysis. The authors acknowledge the High-Performance Computing Platform in PKU for supporting the computational work. Y.L. acknowledges the financial support from National Natural Science Foundation of China (NSFC) (Nos. U1932203 and U1832164).

CONFLICT OF INTEREST STATEMENT

The authors declare no competing financial interest.

ORCID

Yong Lei  <https://orcid.org/0000-0002-4603-7269>

REFERENCES

1. Wu X, Zhang C, Goldberg P, Cohen D, Pan Y, Arpin T, et al. Early pottery at 20,000 years ago in Xianrendong Cave, China. *Science*. 2012;336:1696–700.

2. Rice P. Pottery analysis: a source book. Chicago: University of Chicago Press; 1987.
3. Wood N. Chinese glazes: Their origins, chemistry and recreation. Philadelphia: University of Pennsylvania Press; 1999.
4. Henderson J. The science and archaeology of materials: An investigation of inorganic materials. London: Routledge; 2000.
5. Li J. Science and technology history of China, Vol. Ceramics. Beijing: Science Publishing Company; 1998.
6. Yoshikiyo M, Yamada K, Namai A, Ohkoshi S-I. Study of the electronic structure and magnetic properties of ϵ -Fe₂O₃ by first-principles calculation and molecular orbital calculations. *J Phys Chem C*. 2012;116:8688–91.
7. Tuček Ji, Zbořil R, Namai A, Ohkoshi S-I. ϵ -Fe₂O₃: An advanced nanomaterial exhibiting giant coercive field, millimeter-wave ferromagnetic resonance, and magnetoelectric coupling. *Chem Mater*. 2010;22:6483–505.
8. Machala L, Tuček J, Zbořil R. Polymorphous transformations of nanometric iron(III) oxide: A review. *Chem Mater*. 2011;23:3255–72.
9. Gich M, Gazquez J, Roig A, Crespi A, Fontcuberta J, Idrobo JC, et al. Epitaxial stabilization of ϵ -Fe₂O₃ (001) thin films on SrTiO₃ (111). *Appl Phys Lett*. 2010;96: 112508–112508-3
10. Ohkoshi SI, Imoto K, Namai A, Anan S, Yoshikiyo M, Tokoro H. Large coercive field of 45 kOe in a magnetic film based on metal-substituted epsilon-iron oxide. *J Am Chem Soc*. 2017;139:13268–71.
11. Dejoie C, Sciau P, Li W, Noe L, Mehta A, Chen K, et al. Learning from the past: Rare epsilon-Fe₂O₃ in the ancient black-glazed Jian (Tenmoku) wares. *Sci Rep*. 2014;4:4941.
12. Guan M, Kang B, Wei X, Li G, Jia C, Li H, et al. The microstructure of multicolor hare's fur glaze: The correlation between morphological and compositional characteristics and glaze color. *Heritage Science*. 2021;9. <https://doi.org/10.1186/s40494-021-00498-0>
13. Shen B, Sciau P, Tian W, Brunet M, Li J, Lu W, et al. Micro-structural study of colored porcelains of Changsha kiln using imaging and spectroscopic techniques. *Ceram Int*. 2018;44:18528–34.
14. Liu Z, Jia C, Li L, Li X, Ji L, Wang L, et al. The morphology and structure of crystals in Qing Dynasty purple-gold glaze excavated from the Forbidden City. *J Am Ceram Soc*. 2018;101:5229–40.
15. Liu ZW, Zhang ZG, Li H, Wu W, Hua JJ, Cheng GF, et al. Microstructure characteristics of the black-glazed shreds excavated from the Qingliangsi Kiln. *Key Eng Mater*. 2011;492:112–17.
16. Xu Y, Qin Y, Ding F. Characterization of the rare oil spot glazed bowl excavated from the Xiao kiln site of north China. *Ceram Int*. 2017;43:8636–42.
17. Xu C, Li W, Lu X, Zhang W, Luo H, Guo J. Unveiling the science behind the tea bowls from the Jizhou kiln. Part II. Microstructures and the coloring mechanism. *Ceram Int*. 2018;44:19461–73.
18. Wang L, Wang Y, Zhang M, Li Q, Wu J, Liu Z, et al. Three-dimensional microstructure of ϵ -Fe₂O₃ crystals in ancient chinese sauce glaze porcelain revealed by focused ion beam scanning electron microscopy. *Anal Chem*. 2019;91:13054–61.
19. Wen R, Wang D, Wang L, Dang Y. The colouring mechanism of the brown glaze porcelain of the Yaozhou Kiln in the Northern Song Dynasty. *Ceram Int*. 2019;45:10589–95.
20. Hoo Q, Liang Y, Yan X, Wang X, Tiewa C, Cao X. Millimeter-sized flower-like clusters composed of mullite and ϵ -Fe₂O₃ on the Hare's Fur Jian Ware. *J Eur Ceram Soc*. 2020;40:4340–47.
21. Li G, Wang Z, Zhou J, Kang B, Ding Y, Guan M, et al. The earliest known artificial synthesized ϵ -Fe₂O₃ in the Deqing Kiln ceramic ware of Tang Dynasty. *Heritage Sci*. 2023;11.
22. Chen X, Chen S, Huang R, Zhou X, Ruan M. A study on Song Dynasty Jian Bowl (in Chinese). *Chinese Ceram*. 1983;1:58–66.
23. Kresse G, Furthmüller J. Efficient iterative schemes for ab initio total-energy calculations using a plane-wave basis set. *Phys Rev B*. 1996;54:11169–86.
24. Perdew JP, Burke K, Ernzerhof M. Generalized gradient approximation made simple. *Phys Rev Lett*. 1997;78:1396.
25. Blöchl PE. Projector augmented-wave method. *Phys Rev B*. 1994;50:17953–79.
26. López-Sánchez J, McIntosh G, Osete ML, del Campo A, Villalain JJ, Pérez L, et al. Epsilon iron oxide: Origin of the high coercivity stable low Curie temperature magnetic phase found in heated archeological materials. *Geochim Geophys Geosyst*. 2017;18:2646–56.
27. Namai A, Sakurai S, Nakajima M, Suemoto T, Matsumoto K, Goto M, et al. Synthesis of an electromagnetic wave absorber for high-speed wireless communication. *J Am Ceram Soc*. 2009;131:1170–73.
28. Pravica M, Shen Y, Quine Z, Romano E, Hartnett D. High-pressure studies of cyclohexane to 40 GPa. *J Phys Chem B*. 2007;111:4103–8.
29. Kusano Y, Nakata H, Peng Z, Maki RSS, Ogawa T, Fukuhara M. Studying and utilizing traditional technologies: microstructure and formation mechanism of epsilon-Fe₂O₃ on traditional Japanese Bizen stoneware. *ACS Appl Mater Interfaces*. 2021;13:38491–98.
30. Li X, Lu T. The study on the glisten mechanism of glisten glaze China. *Ceramics (in Chinese)*. 2001;37:14–16.
31. Tanaka M, Niwano K. Silver lustre development of roofing tile glaze from iron oxide. *J Ceram Associat, Japan*. 1973;81:435–40.
32. Westre TE, Kennepohl P, DeWitt JG, Hedman B, Hodgson KO, Solomon EI. A multiplet analysis of Fe K-Edge 1s → 3d pre-edge features of iron complexes. *J Am Ceram Soc*. 1997;119:6297–314.
33. Ahamed I, Ulman K, Seriani N, Gebauer R, Kashyap A. Magnetoelectric ϵ -Fe₂O₃: DFT study of a potential candidate for electrode material in photoelectrochemical cells. *J Chem Phys*. 2018;148:214707.
34. Sans J, Monteseuro V, Garbarino G, Gich M, Cerantola V, Cuartero V, et al. Stability and nature of the volume collapse of ϵ -Fe₂O₃ under extreme conditions. *Nat Commun*. 2018;9.
35. Raupp GB, Delgass WN. Mössbauer investigation of supported Fe and FeNi catalysts: II. Carbides formed Fischer-Tropsch synthesis. *J Catal*. 1979;58:348–60.
36. Li Y, Zhang B, Cheng H, Zheng J. Revealing the coloration mechanism in the earliest Chinese celadon glaze. *J Eur Ceram Soc*. 2019;39:1675–82.
37. Jung J, Shin H-J, Kim Y, Kawai M. Ligand field effect at oxide-metal interface on the chemical reactivity of ultrathin oxide film surface. *J Am Ceram Soc*. 2012;134:10554–61.

38. Krishnamurthy R, Schaap WB. Computing ligand field potentials and relative energies of d orbitals: A simple general approach. *J Chem Educ.* 1969;46:799.
39. Song Z, Liu Q. Basic crystal field theory—A simple and useful tool to understand the structure–property relationship in luminescent materials. *Optical Materials: X.* 2022;16. <https://doi.org/10.1016/j.omx.2022.100189>
40. Li W, Luo H, Li J, Li J, Guo J. Studies on the microstructure of the black-glazed bowl sherds excavated from the Jian kiln site of ancient China. *Ceram Int.* 2008;34:1473–80.
41. Nassau K. 7 -The physics and chemistry of color: The 15 mechanisms.. In: S. K. Shevell, editors. *The science of color.* 2nd ed. Amsterdam: Elsevier Science Ltd; 2003. pp. 247–80.
42. Nassau K. The fifteen causes of color: The physics and chemistry of color. *Color Res Appl.* 1987;12:4–26.

SUPPORTING INFORMATION

Additional supporting information can be found online in the Supporting Information section at the end of this article.

How to cite this article: Guan M, Guo Y, Kang B, Wang M, Li G, Zheng Y, et al. Uncovering the mystery of Al(III) doping of ϵ -Fe₂O₃ in the ancient high-iron black-brown glaze. *J Am Ceram Soc.* 2023;1–12. <https://doi.org/10.1111/jace.19437>